Ceramics International 46 (2020) 403–414

Contents lists available at ScienceDirect

Ceramics International

journal homepage: www.elsevier.com/locate/ceramint

A novel approach for solution combustion synthesis of tungsten oxide nanoparticles for photocatalytic and electrochromic applications

H. Aliasghari[a], A.M. Arabi[b,*], H. Haratizadeh[a,**]

[a] Physics Department, Shahrood University of Technology, 3619995161, Shahrood, Iran
[b] Department of Inorganic Pigments and Glazes, Institute for Color Science and Technology (ICST), Tehran, Iran

ARTICLE INFO

Keywords:
Tungsten oxide
Solution combustion synthesis (SCS)
Organic fuel
Photocatalytic
Electrochromic

ABSTRACT

Tungsten oxide (WO_3) and tungsten oxide hydrate ($WO_3.H_2O$) nanoparticles were synthesized via a novel solution combustion synthesis (SCS) method. Various organic fuels (i.e. oxalic acid, glycine, and citric acid) and heat sources were used to obtain different morphologies of nanoparticles. Combustion thermodynamic relations were explained based on propellant chemistry. Adiabatic temperature (T_{ad}) and specific impulse (I_{sp}) were also obtained. The synthesized nanoparticles were investigated by X-ray diffraction (XRD), Fourier-transform infrared spectroscopy (FTIR), scanning electron microscopy (SEM) and UV–Visible spectrophotometer. XRD patterns indicated that the structures were transformed from orthorhombic and amorphous structures to monoclinic and tetragonal ones, respectively, upon combustion on the hot plate. Fourier-transform infrared (FTIR) spectra provided evidence of WO_6 octahedral. SEM images showed different microstructures from sponge or rock-like to fine spherical particles with up to 100 nm size. The obtained band gap of all samples was higher than 2.6 eV which is the band gap of bulk tungsten oxide. The synthesized WO_3 nanoparticles showed over 50% photocatalytic efficiency for the degradation of azo dye. The results exhibited that the nanoparticles can be used to make the electroactive layer for electrochromic applications.

1. Introduction

Tungsten oxide nanostructures are investigated in various electrochromic [1], photochromic [2] and photocatalytic [3] fields as well as sensors [4], energy storage systems [5,6], etc. due to their applicable properties. Tungsten oxide is a semiconductor transition metal oxide with diverse applications which has attracted the tremendous attention of researchers. WO_3 is a wide band gap semiconductor. The band gap between 2.6 to 3.7eV is reported for various structures of tungsten oxide that can be affected by particle size and shape [7,8]. In some cases, the reported band gap energy is higher than these values. Bulk tungsten oxide exhibits perovskite-like structure and there is tilting from ideal ReO_3 cubic structure by tungsten atoms displacement and oxygen atoms rotation [9,10]. The stoichiometric structures of tungsten oxide share the corners of WO_6 octahedrals which modified as WO_3. The edges of WO_6 octahedrals are shared in the sub-stoichiometric structure. The sub-stoichiometric WO_x composition with $0 < x < 3$ has self-doped oxygen vacancies [10]. The phase transition behavior in nanostructured WO_3 can be quite complex as it mainly depends on the morphology of the materials, which is greatly affected by the nanostructure synthesis process and the initial precursors [11].

The existence of vacancies in the crystal structure is one of the characteristics of tungsten oxide nanostructures that lead to the ability of ion intercalation at vacancies between the O and W bonds. This ability exhibits the changes in the visible color and transparency of this material with respect to the intercalation of small cations such as H^+, Li^+ or Na^+ that is identified as electrochromic properties that are used in smart windows [12–15]. In addition, recent studies have shown the efficiency of tungsten oxide in the photocatalytic degradation of wastewater pollutants through the simple photocatalytic oxidation and reduction mechanism, especially if one considers the tunable band gap energy of tungsten oxide nanostructures [16,17].

Many researchers have examined various methods including hydrothermal [18], acidic precipitation [19], sol-gel and combustion [20,21] techniques for the synthesis of tungsten oxide nanoparticles. The mass production of nanostructures, as well as the shape and size controlling in nanoscale, are the most challenging issues in the synthesis of nanoparticles. Wet chemical methods have the ability to control the morphology of the nanoparticles but the scaling up of these methods is not easy [19]. The main advantage of the combustion

* Corresponding author.
** Corresponding author.
E-mail addresses: aarabi@icrc.ac.ir (A.M. Arabi), hamid.haratizadeh@gmail.com (H. Haratizadeh).

https://doi.org/10.1016/j.ceramint.2019.08.275
Received 2 July 2019; Received in revised form 28 August 2019; Accepted 28 August 2019
Available online 29 August 2019
0272-8842/ © 2019 Elsevier Ltd and Techna Group S.r.l. All rights reserved.

method is its ability for the large scale production of nanoparticles, but the control of morphology is difficult due to the high temperature and reaction rate in this method [17–19]. The heat released from the chemical reaction or electron transferring between the fuel and the oxidizer in combustion reaction is used for material synthesis [20]. Indeed, the combustion synthesis is an exothermic redox reaction. Generally, it is an interaction between water-soluble metal nitrates as the oxidizer and organic fuels (such as glycine, glucose, etc.) which can occur in liquid or solid state [22].

The common approaches for combustion synthesis include self-propagation high temperature synthesis (SHS), in which high speed reaction of precursors is done in the solid state, and solution combustion synthesis method (SCS) [22,23]. The exothermic self-propagating reaction was first introduced about 50 years ago. The primary research studies in this field were started by Merzhanov in Russia in the late 1960s [22]. The SHS is so exothermic ($T_{ad} \sim 4000\,^{\circ}C$) and self-propagating that results in coarse products. The SHS is a high-temperature solid-state method which makes it difficult to control the phase purity and particle size. So, it is not suitable for the synthesis of nanostructured materials. A low-temperature combustion method was developed by Patil et al. for the first time [22]. The solution combustion process leads to the synthesis of metal oxides by rapidly heating an aqueous solution containing stoichiometric quantities of the precursors [24]. Stoichiometry calculation is very important and critical to solution combustion synthesis [25]. The principles of propellant chemistry are used to calculate the stoichiometry of the reaction that is based on balancing elemental oxidizing and reducing valences of the utilized compounds in the combustion reaction [26].

In this work, a novel SCS method was used as a versatile, mass production and low cost technique for the synthesis of tungsten oxide nanoparticles. Afterward, photocatalytic activities of the nanoparticles and the electrochromic application of RF-sputtered thin films were also studied.

2. Experimental procedure

2.1. Chemicals and reagents

Tungsten metal powder (analytical grade, 99.99% purity) was purchased from Sigma Aldrich. Hydrogen peroxide (H_2O_2, 30% purity), HNO_3(67%), H_2SO_4 (37%), oxalic acid ($C_2H_2O_4$), glycine ($C_2H_5NO_2$), citric acid ($C_6H_8O_7$) and Reactive Blue 194 azo dye (REA.BLUE 4GX, MEGHMANI) were provided from Merck (Germany).

2.2. Nanoparticles synthesis

The synthesis of nanoparticles was done via two simultaneous reactions. While tungsten oxide nanoparticles were synthesized via one reaction, the other was reacted as a combustion to provide the required heat for the final formation of $WO_3.H_2O$ or WO_3 nanoparticles. Initially, 8.0 gr tungsten powder was dissolved in certain amounts of hydrogen peroxide. The addition of H_2O_2 was continued until the tungsten was completely dissolved and the solvent became clear. The reactions are as follow [27,28]:

$$W(s) + 3H_2O_2(l) \rightarrow H_2WO_4(aq) + 2H_2O(l) \quad (1)$$

$$H_2WO_4(aq) \rightarrow WO_3.H_2O(s) \text{ or } WO_3(s) + H_2O(g) \quad (2)$$

The product of equation (1) was tungstic acid. An exothermic combustion reaction was also used in parallel to provide the required heat (Δ) for the formation of nanoparticles in equation (2) [29,30]. The theoretical reactions for releasing the heat for the formation of $WO_3.H_2O$ and WO_3 can be written as follow:

$$2HNO_3(aq) + 5C_2H_2O_4(s)(\text{Oxalic acid}) \rightarrow 10CO_2(g) + 6H_2O(g) + N_2(g) \quad (3)$$

$$9HNO_3(aq) + 5C_2H_5NO_2(s)(\text{Glycine}) \rightarrow 10CO_2(g) + 17H_2O(g) + 7N_2(g) \quad (4)$$

$$18HNO_3(aq) + 5C_6H_8O_7(s)(\text{Citric acid}) \rightarrow 30CO_2(g) + 29H_2O(g) + 9N_2(g) \quad (5)$$

As a typical procedure, 18.0 mL HNO_3 and 82.0 gr oxalic acid ($C_2H_2O_4$) was added to the solution of tungsten powder in H_2O_2. The prepared solution was then heated in a beaker on a hot plate at 80 °C to obtain a viscous gel. Then the ignition was done directly on hot plate through burn with flame leading to the formation of the HO sample (maximum temperature of the hot plate was 200 °C). The combustion on the hot plate was linear for all fuels. In linear combustion, the burning surface recedes from top to bottom layer by layer. Other samples of H–series, including HG and HC, were synthesized using glycine ($C_2H_5NO_2$) and citric acid ($C_6H_8O_7$) fuels on a hot plate, respectively. The combustion of glycine was done with no flame exiting the gases and ashes, so the powder had a black appearance. The citric acid had a slow combustion rate and there were brown-color gases with no ash and flame. In another way, the as-prepared gel was transferred to the muffle furnace and the combustion process was performed at 550 °C for 2 h which led to the formation of WO_3 nanoparticles of F–series. Heating in the furnace leads to the combustion of fuels entire the volume with flame and the products have a pure green appearance finally [22]. The same procedure was used for other fuels. Table 1 lists the details of the samples with respect to the heat source and fuel type.

2.3. Characterization

Crystal structure of the synthesized samples was studied by X-ray powder diffraction using PHILIPS-PW1730 X-ray diffractometer with Cu-Kα radiation (λ = 1.54056 Å) at 2θ range of 10°-80° and step size of 0.05. Bondings and functional groups in samples were investigated by Fourier-transform infrared (FTIR) spectroscopy using PerkinElmer spectrometer in a KBr matrix. SEM (LEO 1455vp) was used to determine the surface morphology of the nanoparticles. UV–Vis spectra of the powders were recorded at room temperature with a double beam spectrophotometer (PerkinElmer UV–Vis Lambda 20) over the wavelength of 200–800 nm. Cyclic voltammetry (CV) was used to exhibit the electrochromic behavior of the selected sample (Autolab Potentiostat Palm Sens 3).

Table 1
Characteristics, codes and structural data of different samples.

Sample	Heat source	Fuel type	Structure-JCPDS card	Crystallite size(nm)
HO	Hot plate	Oxalic acid	Orthorhombic 01-084-0886	18.4 nm
HG	Hot plate	Glycine	Amorphous	–
HC	Hot plate	Citric acid	Orthorhombic 01-084-0886	11.5 nm
FO	Furnace	Oxalic acid	Monoclinic 01-088-0545	22.9 nm
FG	Furnace	Glycine	Tetragonal 01-085-0808	16.7 nm
FC	Furnace	Citric acid	Tetragonal 01-085-0808	18.3 nm

2.4. Photocatalytic reaction

The photocatalytic activity of the synthesized semiconductors was evaluated using the oxidative decomposition of double Reactive Blue 194 azo dye in aqueous solution. RB 194 is an anionic dye mainly used for dyeing of cotton and viscous fibers in textile industries. The experiments were carried out in an annular semi-batch photoreactor (internal volume of 320 ml, Pyrex) equipped by a 15 W low-pressure mercury lamp (OSRAM, λ = 253.7 nm). A quartz tube was used as a lamp protector inside the reactor. The released photons were able to supply 4.88 eV energy.

2.5. Electrochromic thin film preparation

Tungsten oxide thin films were prepared by RF sputtering of HG and FG targets at 1.5×10^{-2} torr, 150 W and argon gas flow rate of 5 sccm. The sputtering time was 90 min. The FTO-glass was used as a conductive transparent substrate. The tungsten oxide target (50 mm in diameter and 3 mm in thickness) was made by pressing the synthesized HG and FG powders.

3. Results and discussion

3.1. Thermodynamic calculations

Theoretical calculations of the combustion reaction between nitric acid (HNO_3) and the fuels are done based on the heat of formation of reactants and products [22,31]. Extremely high temperatures over 1550 °C can be produced in solution combustion reactions in a short time. So, it can be assumed that there is a thermally isolated system. The maximum temperature of the product is assumed to be the adiabatic temperature (T_{ad}). In the combustion reaction, the adiabatic temperature is equal to the flame temperature and evaluates the reaction strength. The liberated heat during the reaction is the enthalpy of the system and is a state function that is expressed as equation (6) [21,31]:

$$\Delta H^0 = \Delta H_f^0 = \int_{298}^{T_{ad}} \sum n \Delta C_p(product) dT \quad (6)$$

The heat released during the synthesis of tungsten oxide by combustion of HNO_3 and fuel mixtures can be calculated using equation (7) for ΔH_f^0 values (each being multiplied by its respective stoichiometric coefficient, n) of the reactants and products (heat of formation in kcal. mol^{-1}) at STP.

$$\Delta H_f^0(reaction) = \sum n \Delta H_f^0(product) - \sum n \Delta H_f^0(reactants) \quad (7)$$

where ΔH^0 is the combustion reaction heat, n is the number of moles of reactants, C_p is the specific heat and ΔH_f^0 is the heat of formation at 298 K. The adiabatic temperature is calculated by interpolation of equation (7) in (6). The T_{ad} for various fuels is presented in Table 2. The released energy during combustion is given as the specific impulse (I_{sp}) of a propellant [32]. The I_{sp} determines the reaction ignition intensity which can be calculated by equation (8) [21,31]:

$$I_{sp} = k \sqrt{\frac{T_{ad}}{\text{the number of moles of gaseous products}}} \quad (8)$$

where k is the Boltzmann constant.

3.2. Structural studies

The room temperature XRD patterns of as-synthesized tungsten oxide nanoparticles are shown in Fig 1. HO and HC samples show the same XRD patterns corresponding to the orthorhombic crystal structure (JCPDS card no. 01-084-0886) of tungsten oxide hydrate ($WO_3.H_2O$). The HC sample has lower crystallinity due to the dual function of citric acid as fuel and chelating agent [33]. The HG sample shows the pattern of amorphous structures.

XRD patterns of samples prepared in the furnace as a heat source are changed dramatically from the $WO_3.H_2O$ phase to pure WO_3. Although FO is monoclinic (JCPDS No. 01-088-0545), FG and FC samples show tetragonal crystal structure (JCPDS No. 01-085-0808). Because of 2 h heat treatment at 550 °C, there are no peaks of impurities, intermediates or other compounds in the F-series samples and they show higher crystallinity than the H-series ones. It seems that the higher energy of ignition in the furnace led to the irreversible orthorhombic to tetragonal phase transformation in WO_3 [34,35]. However, the final structure in FO is monoclinic and this means that the ignition of oxalic acid is not high enough for phase transformation toward tetragonal structure (the stable structure at high temperature > 740 °C) [36]. It is in good agreement with the lowest adiabatic temperature, the volume of exhaust gases and the I_{sp} of the oxalic acid combustion reaction. The crystallite size of the nanoparticles is determined by the Scherrer equation as shown in Table 1 [19,37]. The average crystallite size of the as-synthesized samples is less than 25 nm, so it can be assumed that the grain size is equal to crystallite size. It can be seen that the F-series have higher crystallite size than the H-series ones due to more soaking time at the higher temperature.

3.3. FTIR spectra

The FTIR spectra of the samples are shown in Fig. 2 and the peaks are listed in Table 3. The main differences between H and F samples are lowering of the OH bands and intensifying the WO_6 octahedral peaks. In all samples, the strongest peaks in the range of 400–1000 cm^{-1} belong to the typical vibrations of WO_6 octahedral which are pureed and intensified in the F-series. The peaks at ~1080 cm^{-1} and ~980 cm^{-1} correspond to W–O–C and W═O stretching vibrations in HO, HG and HC samples [38–40]. The other bond by stretching vibration assignment of O–W is presented at 764 cm^{-1} and 724 cm^{-1}wavelengths. The small shift in the vibrational frequencies may be due to the surface effect [38]. The other bands are due to the splitting of resulted from the nearest neighbor interaction.

The disappearance of peaks at ~1720 cm^{-1} and ~1240 cm^{-1} in HG, HC, FG and FC samples is related to the lack of oxalic acid as the precursor. In the case of FO sample, the oxalic acid is used in the reaction but decomposes at high temperature as CO_2 gas.

3.4. Morphological studies

SEM images and photos of the samples synthesized on the hot plate are shown in Fig. 3. The microstructure and the appearance of the samples differ greatly due to the change in fuel type. The HO sample has a yellowish green color and contains spherical nanoparticles with

Table 2
Calculated thermodynamic values for different fuels.

Fuel type	Oxidizer to fuel ratio	Volume of exhaust gases (mol)	$\Delta H^0_{Combustion}$ (kJ/mol)	T_{ad} (°K)	I_{sp} (°K/mol)$^{0.5}$*10^{-23}
Oxalic acid ($C_2H_2O_4$)	0.4	25	−826	1025.8	1.8625
Glycine ($C_2H_5NO_2$)	1.8	34	−3539	2438.2	2.3471
Citric acid ($C_6H_8O_7$)	3.6	68	−7364	2526.7	1.5620

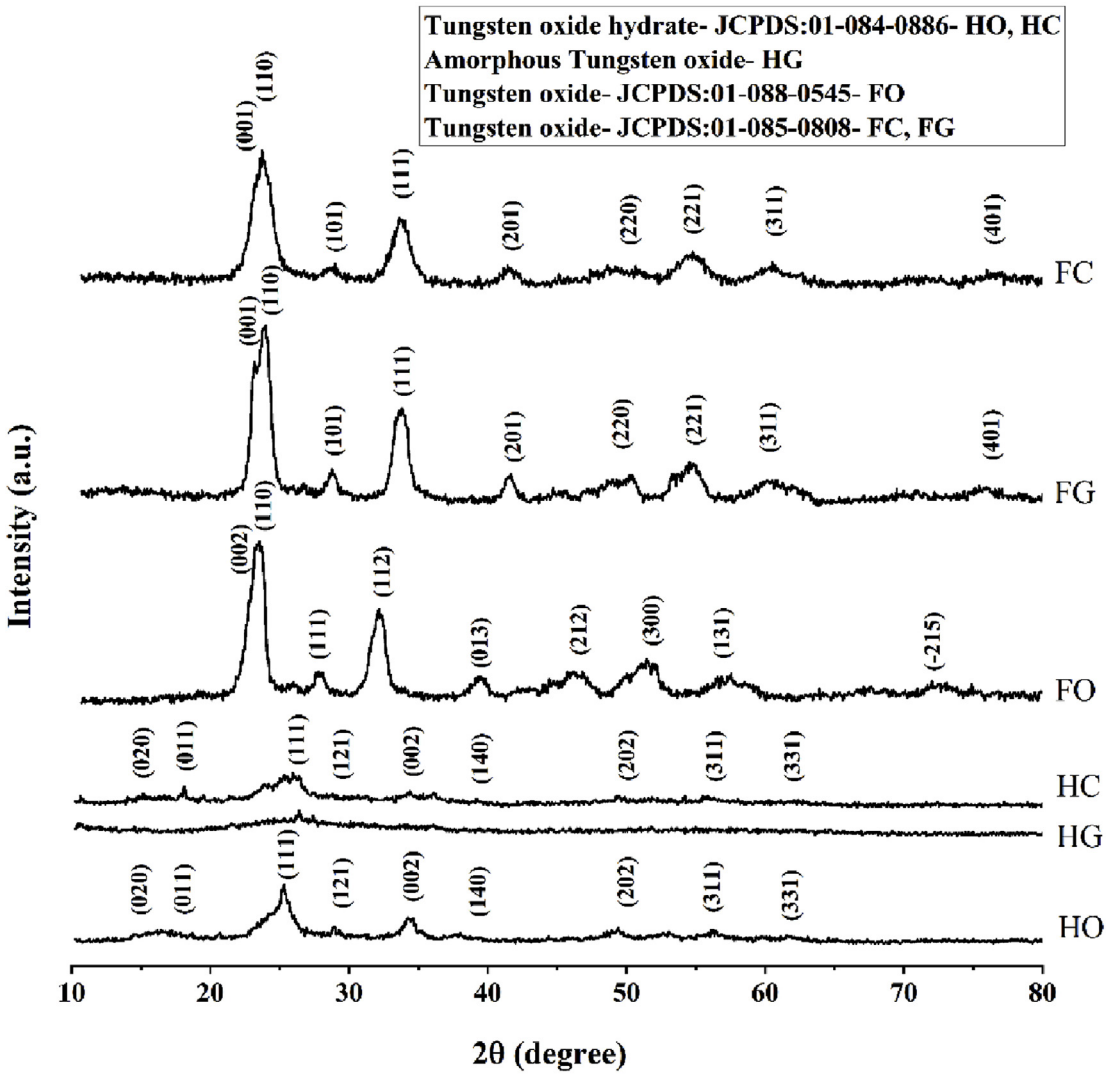

Fig. 1. XRD patterns of the synthesized samples.

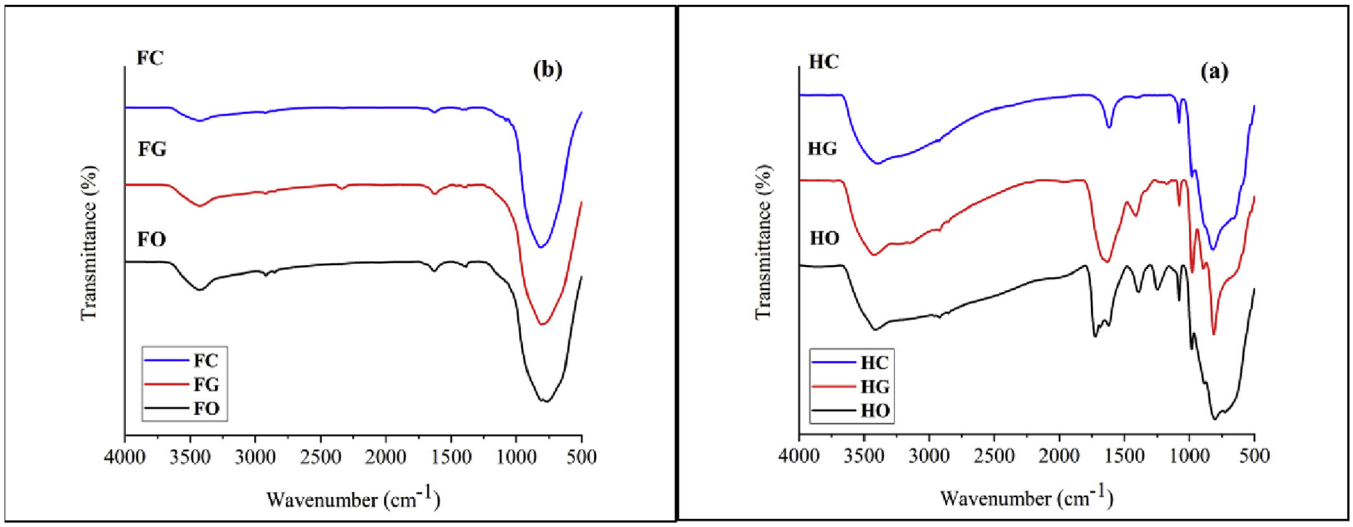

Fig. 2. FTIR spectra of (a) HO, HG, HC, and (b) FO, FG, FC samples.

Table 3
Band positions of FTIR spectra.

Sample by band position(cm^{-1})						Band assignment	references
HO	HG	HC	FO	FG	FC		
3415.46	3429.63	3399.67	3431.33	3431.49	3432.40	υ_{sym} and υ_{asym} of OH	[38]
2920.63	2923	2929	2920	2930	2895	υ_{sym} and υ_{asym} of (CH_2)	[39,59]
				2339		N=C=O	[31]
1723.99						υ_{asym} (COO)	[38]
1620.65	1630.29	1616.10	1627.64	1625.58	1627.11	δ (H–O–H)	[31,38]
1398	1412.28	1405	1395	1402	1410	δ (CH_2)	[59]
1247.63						υ_{sym} (COO)	[38]
1079.85	1078.82	1080.8				υ (W–O–C)	[38]
982.09	979.26	981.13				υ (W=O)	[38–40]
887	894.40					υ (O–O) and υ (W–O_{inter}–W)	[39,60]
803.00	813.09	819.19	810	809.12	814.86	υ(W–O_{intra}–W)	[39,60]
724			764.24			υ (O–W)	[60]
	673	687				υ_{asym} (W–O)	[40]

an average particle size of about 200 nm. The sponge-like morphology can only be seen in the HG sample. The black appearance can be related to the residual carbonaceous material. The pore size of the HG sample varies in a wide range from 100 nm to 1 μm. HC sample has a deeper yellow color and consists of up to 100 nm spherical tungsten oxide nanoparticles. More uniformity of particles in these samples can be assigned to the dual function of citric acid as an organic fuel and chelating agent [33].

SEM images and photos of the samples synthesized in the furnace are shown in Fig. 4. All furnace samples have a deeper green appearance. Except for FO, other samples show a well-grown microstructure. Because of gradual heating and cooling in the furnace, FO reversibly transformed into the monoclinic structure (room temperature structure) in the cooling step. On the other hand, the ignition of oxalic acid is not as energetic as other fuels, so the sample could not receive the required energy to transform into the irreversible stable tetragonal phase. Because of the expansion and contraction of the structure, the sample shows finer particle size distribution. FG sample consists of the coarse-grained porous structure. Because of the presence of amine groups in glycine [41], combustion in glycine is more

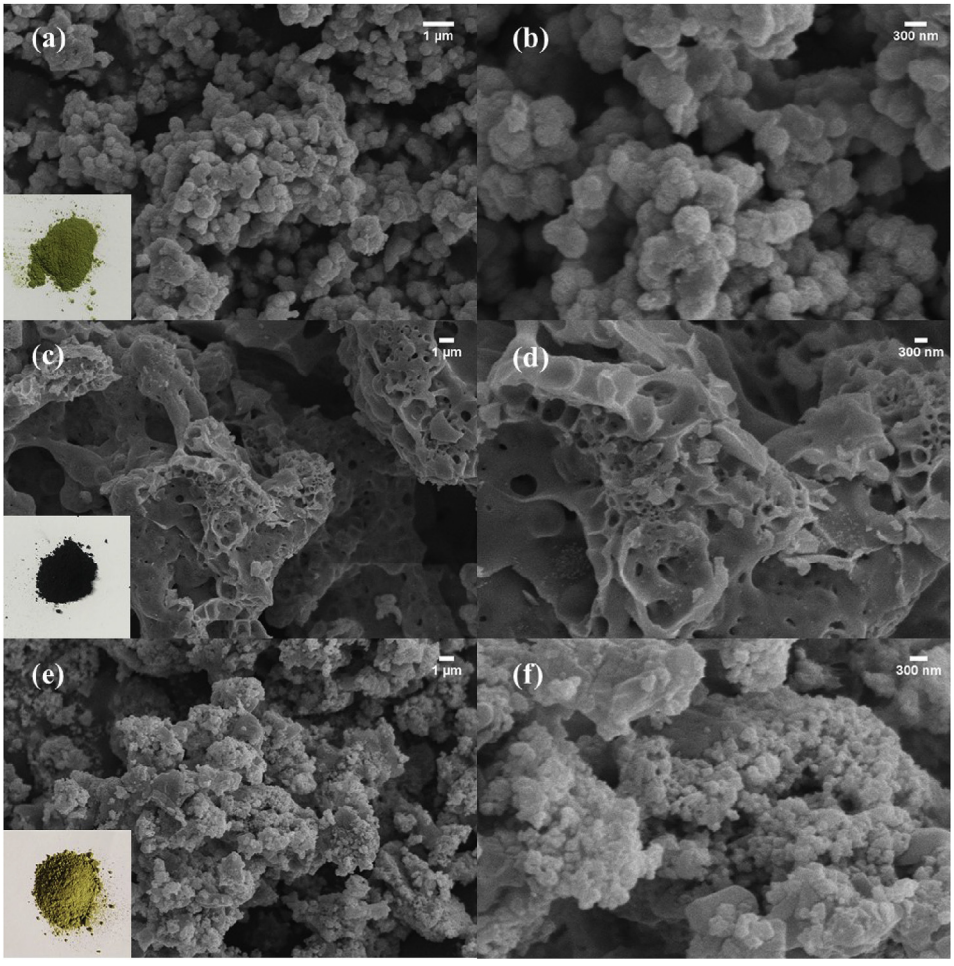

Fig. 3. SEM images of (a, b) HO, (c, d)HG, and (e, f) HC samples.

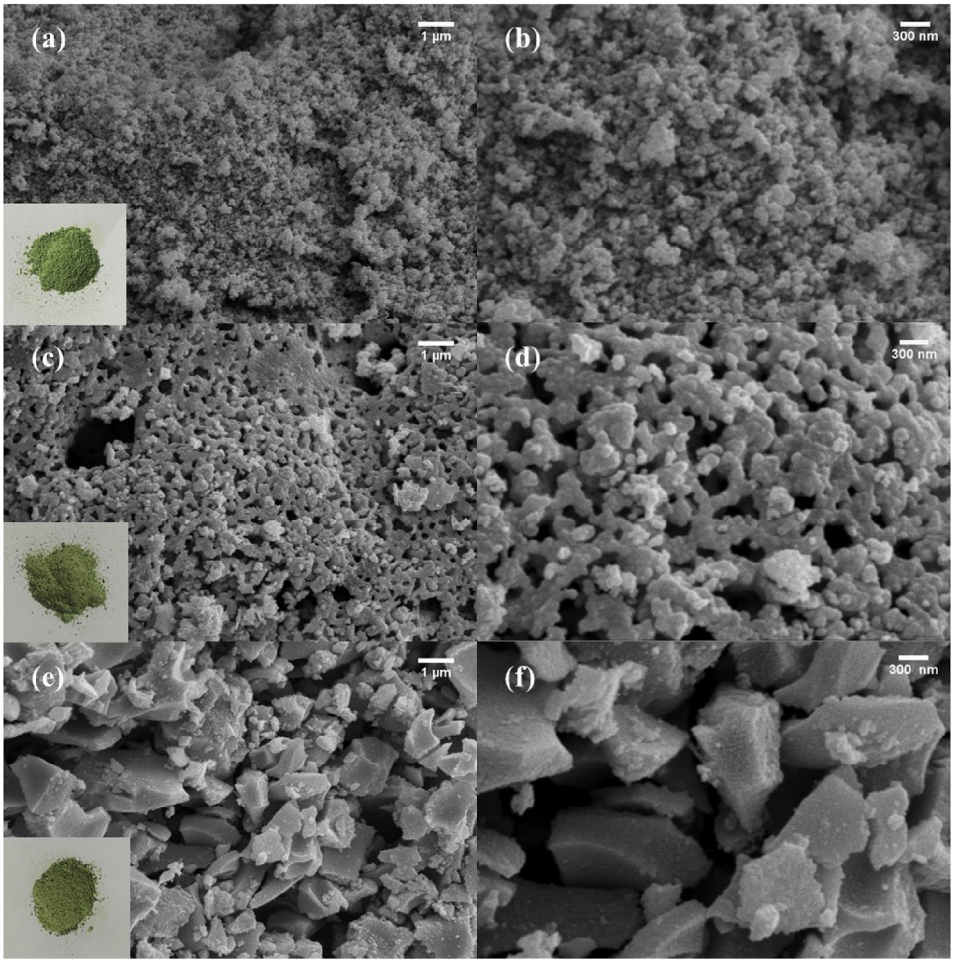

Fig. 4. SEM images of (a, b) FO, (c, d) FG, and (e, f) FC samples.

sparkling than integrated combustion. As a result, sequential ignitions lead to the sponge-shaped morphologies. In the next step, semi-sintered particles are formed in the sponge-like agglomerates during the gradual heating and cooling in the furnace. FC sample has a rock style with large particles. It is known that citric acid fuel plays two roles: providing the required heat through combustion reaction (equation (5)), and the chelating effect. As a result of the combustion in the presence of citric acid, ultra-fine primary particles are formed which are further coarsened to the rock-like particles in the furnace on the basis of Ostwald ripening theory [42].

In general, the different morphologies and particle sizes of the synthesized nanoparticles result from the heat source and the fuel type. The created pores in the powders are related to the volume of the exhaust gases (T_{ad} and I_{sp} of the reactions according to equations (3)–(5) and Table 2). The heat source also obtains the combustion propagation type that can be lamellar (layer by layer) or in volume. The hot plate leads to layer by layer ignition and the furnace leads to volume combustion [22]. It can be found from XRD and SEM results that the crystal structure transforms from metastable (orthorhombic or amorphous in HO, HG and HC samples) to more stable room temperature (monoclinic in the FO sample) or high temperature (tetragonal in FG or FC samples) by the change of heat source from rapid heating and cooling method (hot plate) to the gradual one (furnace) [9,10]. As mentioned above, the suggested mechanism and application process are shown are shown in Fig. 5.

3.5. Optical properties

Transmittance spectra of the nanoparticles are shown in Fig. 6. The optical band gap of the materials can be obtained by the relation between the absorption coefficient and intercalated photon energy as equation (9) [43,44]:

$$\alpha h\upsilon = k(h\upsilon\text{-}E_g)^n \quad (9)$$

where k is constant, E_g is the band gap energy, $h\upsilon$ is the photon energy and α is the absorption coefficient. The value of n is determined by the type of the optical band gap that can be 1/2, 2, 3/2 and 3 for direct allowed, indirect allowed, forbidden direct and forbidden indirect band gaps, respectively. The bulk tungsten oxide mainly is an indirect band gap semiconductor and has no photoluminescence emission [45]. However, according to studies on the properties of tungsten oxide, both direct and indirect band gap have been reported for tungsten oxide nanostructures. Assuming a direct band gap for tungsten oxide nanostructure, the considered value for n is 1/2 [46–52]. When the reflectance of the material is low, the absorption coefficient without considering the reflectance is given by equation (10):

$$\alpha = -1/t\ \mathrm{Ln}T \quad (10)$$

where T is the transmittance and t is the thickness of the sample. In the Tauc method, a straight line is fitted to the linear part of $(\alpha h\upsilon)^2$ curve versus $h\upsilon$ and the band gap energy is determined from extrapolating the fitted line. The tauc plots are shown in Fig. 7. The band gap energies of HO, HG and HC samples are 3.9 eV, 3.25 eV, and 4.0 eV and those of FO, FG and FC samples are 3.8 eV, 3.2 eV, and 3.6 eV, respectively.

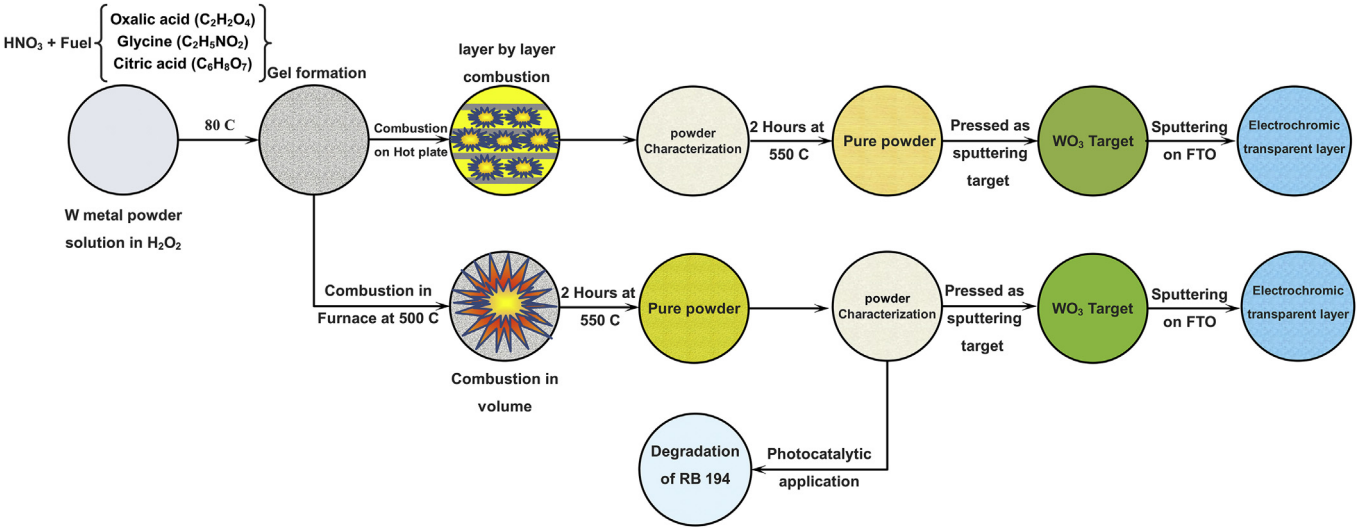

Fig. 5. Schematic diagram for the synthesis of tungsten oxide nanoparticles and their applications.

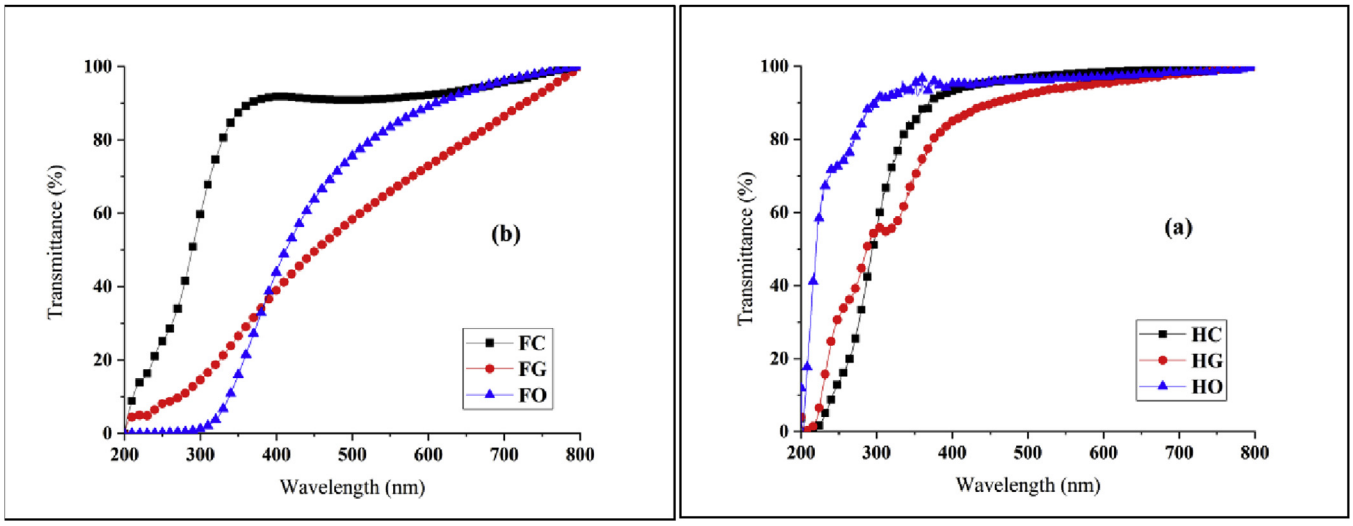

Fig. 6. The transmittance spectra in the UV–Visible range for (a) HO, HG, HC, and (b) FO, FG, FC samples.

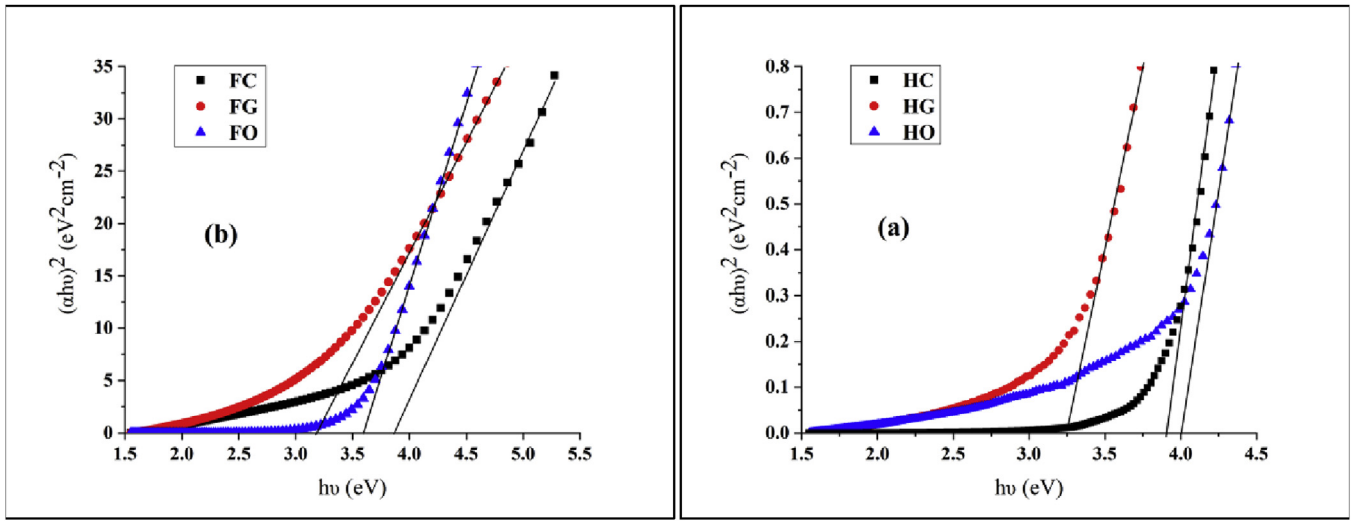

Fig. 7. Tauc plot and calculation of band gap for(a) HO, HG, HC, and (b) FO, FG, FC samples.

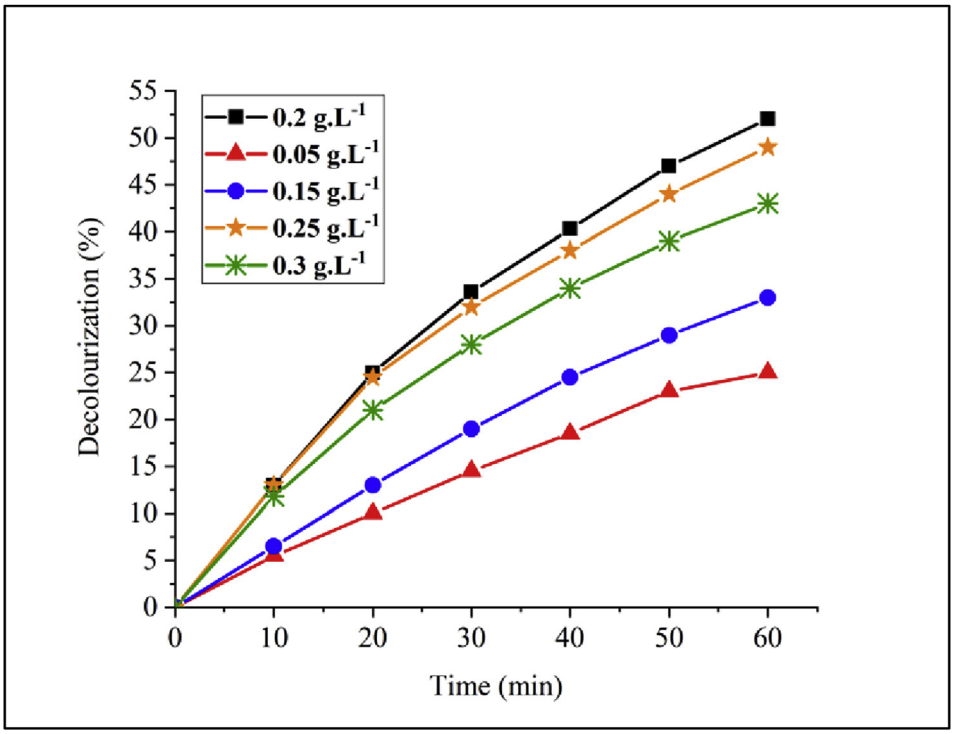

Fig. 8. Effect of catalyst dose on photocatalyticdegradation of RB (T = 23 °C, initial dye concentration: 20 mgr L^{-1}, dye solution pH 7).

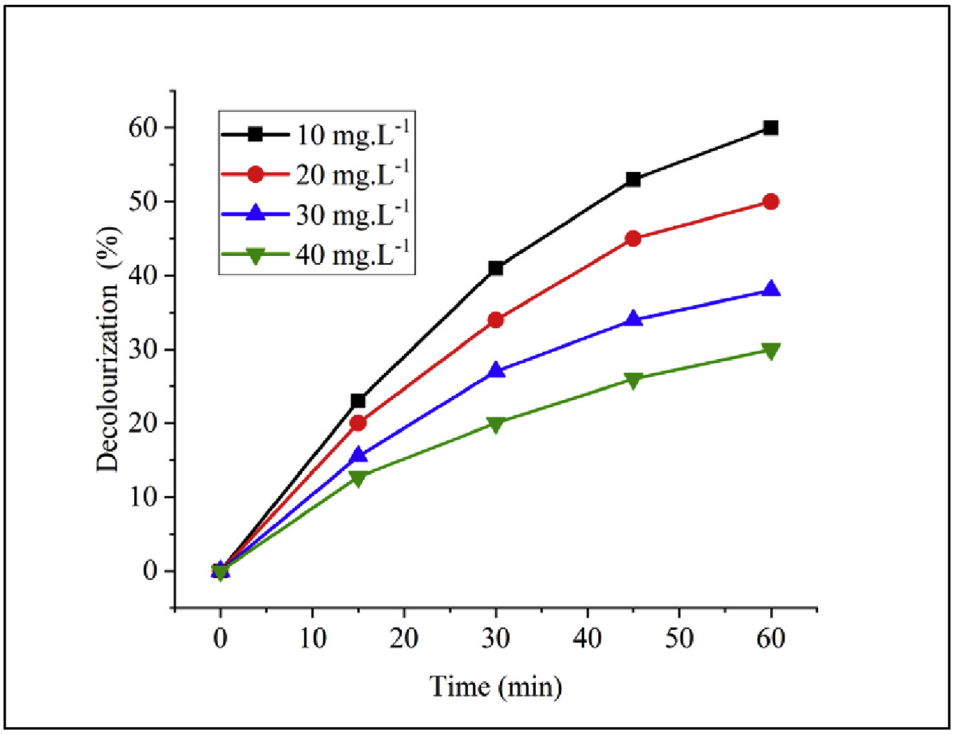

Fig. 9. The effect of initial dye concentration on dye photodegradation (catalyst dose: 0.2 gr L^{-1}, pH 7).

3.6. Applications

3.6.1. Degradation procedure

The aqueous dye solution was prepared by dissolving an appropriate amount of the dye powder in a specific volume of pure water. The pH of the dye solution was adjusted using HCl and NaOH. A weak pump was used to circulate the dye solution through the reactor. The dark adsorption of the sample was investigated by keeping the solution in the dark for 20 min; thereafter the UV lamp was turned on. The samples were taken from the reservoir tank at different time intervals and centrifuged at 4500 rpm for 7 min. Then the light absorption spectra of the solution were monitored using a UV–Visible spectrophotometer. The decolorization of the solution can be calculated by the following equation:

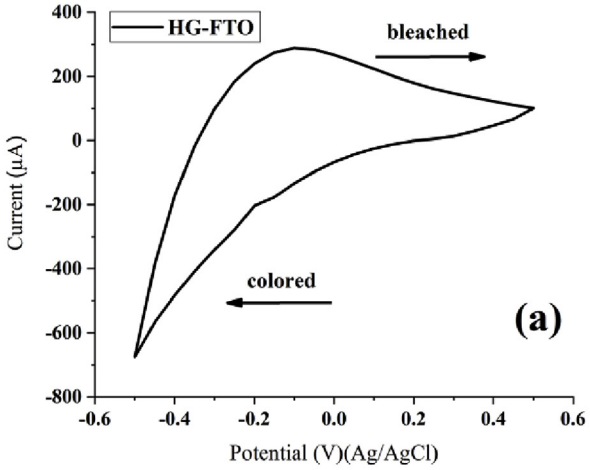

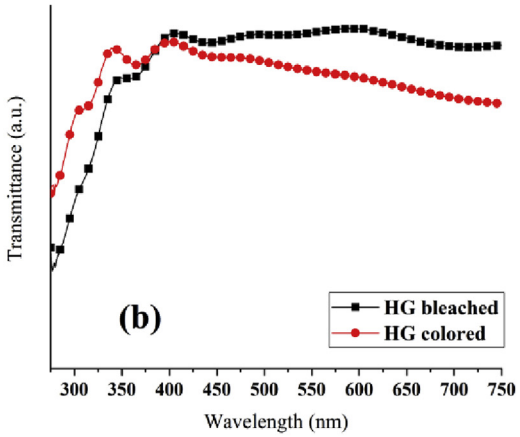

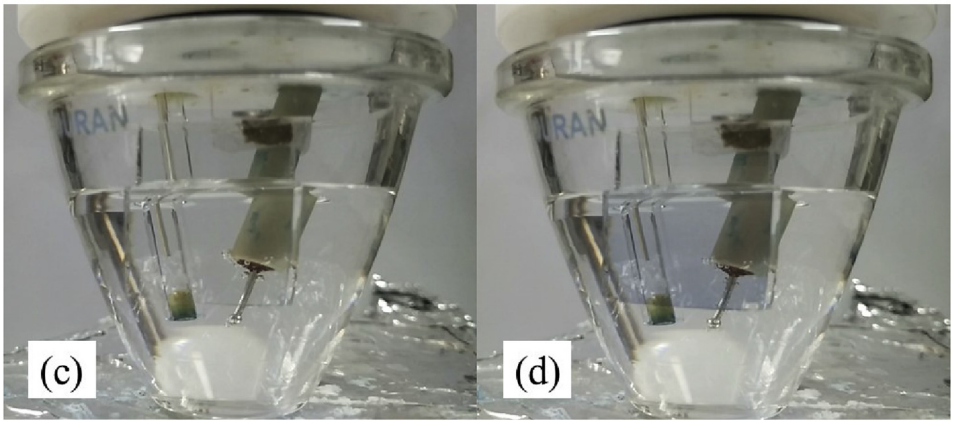

Fig. 10. (a)Cyclic Voltammetry of HG coated on FTO,(b) transmittance spectra(c) bleached state and (d) colored state.

$$Dec(\%) = \frac{A_0 - A}{A_0} \times 100 \quad (11)$$

where A_0 and A are the light absorbance before photocatalytic reaction and after the reaction for time t, respectively. The photodegradation of RB molecules in aqueous solution under UV irradiation was investigated to evaluate the photocatalytic activity of the as-prepared sample. The effect of catalyst dose and initial dye concentration were investigated as the most important parameters on the photocatalytic reaction.

3.6.1.1. Effect of catalyst dose on the photocatalytic reaction. The photocatalytic experiments with different loading amounts of catalyst (from 0.05 gr L^{-1} to 0.30 gr L^{-1}) and the initial dye concentration of 20 mgr L^{-1} of solution for 60 min reaction time were carried out to determine the optimum catalyst dose. Increasing the catalyst dose from 0.05 gr L^{-1} to 0.2 gr L^{-1} increased the number of catalyst active sites and produced more hydroxyl radicals, consequently increasing the rate of reaction [53]. At a specific point, the photocatalytic efficiency starts to decrease by increasing the catalyst dose to 0.25 gr L^{-1}. This behavior could be explained by the fact that the catalyst particles caused light

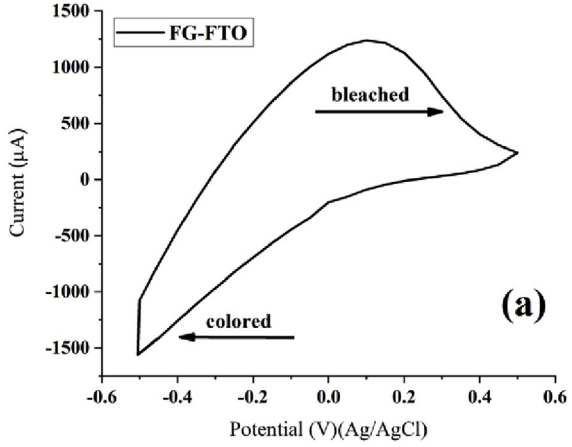

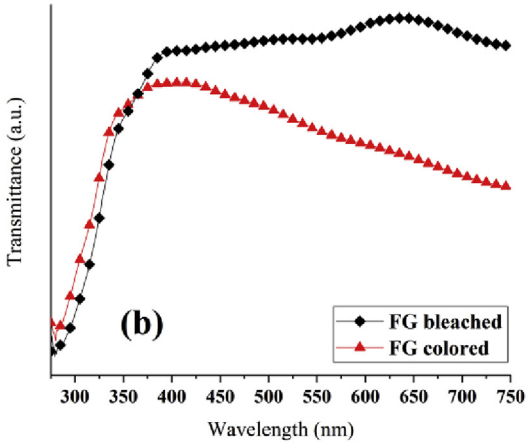

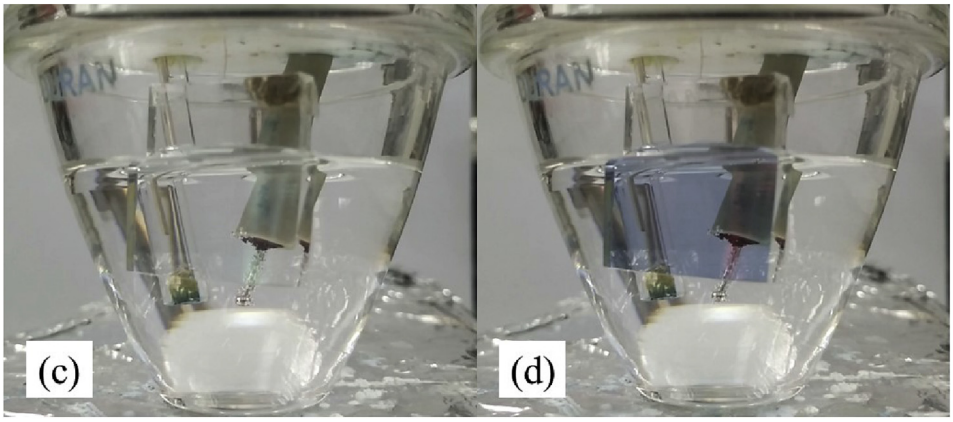

Fig. 11. (a) Cyclic Voltammetry of FG coated on FTO, (b) transmittance spectra (c) bleached state and (d) colored state.

scattering which resulted in reducing the photons absorbed by the catalyst surface [54]. On the other hand, the agglomeration of particles occurs by increasing the amount of catalyst [55]. As can be seen in Fig. 8, the best decolorization of 20 mgr L^{-1} of RB solution was obtained in the presence of 0.2 gr L^{-1} of WO_3 nanopowders where 53% of decolorization was achieved within 60 min.

3.6.1.2. Effect of initial dye concentration on the dye photodegradation. The photodegradation of RB was studied with four different initial dye concentrations at pH 7 in the presence of 0.2 gr L^{-1} of catalyst powder. Fig. 9 shows the decreasing of dye photodegradation by increasing the initial dye concentration from 10 mgrL^{-1} to 40 mgr L^{-1}. The presumed reason is that increasing the initial dye concentration would consequently decrease the light path length and prevent the light to be absorbed by the surface of the catalyst particles [56,57]. On the other hand, the increase of pollutants in the constant $^{\bullet}OH$ radical production by means of constant catalyst dose leads to the reduction of dye photodegradation [56]. The results

showed the effective photocatalytic degradation of low concentration dye solutions. This fact introduces the photocatalytic treatment as a supplementary wastewater treatment when the water pollutants are diluted using the primary treatment methods.

3.6.2. Electrochromic studies

Smart windows as electrochromic devices are one of the most favorable applications of tungsten oxide. In this work, the synthesized HG and FG samples were selected for the electrochromic application comparison. The synthesized samples were coated on FTO (Fluorine-doped tin oxide) glass substrate as an active electrochromic layer using the RF-Sputtering method. Hydrogen ion (H^+) intercalation/deintercalation characterization in potentiostatic mode was conducted in a three-electrode electrochemical cell with 0.1 M H_2SO_4 as a liquid electrolyte Ag/AgCl as reference electrode and Pt wire as the counter electrode. The coloration of the HG film was carried out at −0.6 V with respect to the reference electrode, while bleaching was performed at 0.6 V. The Cyclic voltammetry diagram verified the reduction (colored) and oxidation (bleached) states of the HG thin film as can be seen in Fig. 10 (a) [58]. Transmittance spectra were recorded for bleached and colored states of HG film that are shown in Fig. 10 (b). The difference in the transmittance of bleached and colored states is approved by the electrochromic application of the samples. Fig. 10 (c,d) exhibits the bleached and colored of the prepared HG Film.

The FG film was prepared for comparing the electrochromic application. The preparation condition was similar to the HG film. The Cyclic voltammetry diagram, Transmittance spectra and the photos of bleached and colored states are exhibited in Fig. 11 (a), (b) and (c,d), respectively. Comparing Figs. 10 and 11 revealed that the FG sample has a better response to the applied potential. It can be seen in cyclic voltammetry results that the intercalated ions in FG are about three times larger than the HG.

4. Conclusions

A novel solution combustion route (SCS) was introduced to synthesize tungsten oxide nanoparticles. X-ray diffraction patterns indicated that combustion on the hot plate was suitable for the preparation of orthorhombic and amorphous $WO_3.H_2O$ whereas combustion in the furnace was suitable for achieving stable tetragonal high-temperature WO_3 structures. SEM images confirmed the ability of this method for the preparation of different morphologies such as sponge-like, rock style, spherical or irregular shapes. FTIR and XRD results approved the influence of fuel type on the synthesis of tungsten oxide (WO_3) and tungsten oxide hydrate ($WO_3.H_2O$) nanoparticles via a furnace and hot plate, respectively. The ability of the synthesized powders for degradation of reactive blue (RB) under UV irradiation was also studied. The best decolorization value of 53% was obtained for 20 mgr L^{-1} of RB dye in the presence of 0.2 gr L^{-1} of WO_3 for 60 min. Finally, the electrochromic application of the prepared thin films was proved using cyclic voltammetry (CV) in the H_2SO_4 electrolyte. The results exhibited that both HG and FG samples have a good electrochromic response. The FG sample showed better response at the same potential due to its crystalline structure.

References

[1] F. Blanchard, B. Baloukas, L. Martinu, Highly durable electrochromic tungsten oxide thin films prepared by high rate bias-enhanced sputter deposition, Appl. Mater. Today. 12 (2018) 235–243, https://doi.org/10.1016/j.apmt.2018.05.001.

[2] D. Ding, Y. Shen, Y. Ouyang, Z. Li, Hydrothermal deposition and photochromic performances of three kinds of hierarchical structure arrays of WO_3 thin films, Thin Solid Films 520 (2012) 7164–7168, https://doi.org/10.1016/j.tsf.2012.08.003.

[3] D. Vernardou, H. Drosos, E. Spanakis, E. Koudoumas, C. Savvakis, N. Katsarakis, Electrochemical and Photocatalytic Properties of WO_3 Coatings Grown at Low Temperatures, (2011), pp. 513–517, https://doi.org/10.1039/c0jm02413a.

[4] W. Zeng, B. Miao, T. Li, H. Zhang, S. Hussain, Y. Li, W. Yu, Hydrothermal synthesis, characterization of h- WO_3 nanowires and gas sensing of thin film sensor based on this powder, Thin Solid Films 584 (2015) 294–299, https://doi.org/10.1016/j.tsf.2014.12.037.

[5] W. Li, Z. Fu, Applied Surface Science Nanostructured WO_3 thin film as a new anode material for lithium-ion batteries 256 (2010) 2447–2452, https://doi.org/10.1016/j.apsusc.2009.10.085.

[6] J. Zhao, Y. Tian, Z. Wang, S. Cong, D. Zhou, Q. Zhang, M. Yang, W. Zhang, F. Geng, Z. Zhao, Communications electrochromic batteries hot paper trace H_2O_2 -assisted high-capacity tungsten oxide electrochromic batteries with ultrafast charging in, Seconds Angewandte 215123 (2016) 7161–7165, https://doi.org/10.1002/anie.201602657.

[7] D.B. Migas, V.L. Shaposhnikov, V.N. Rodin, V.E. Borisenko, Tungsten oxides . I . Effects of oxygen vacancies and doping on electronic and optical properties of different phases of WO_3, J. Appl. Phys. 108 (2010) 1–7, https://doi.org/10.1063/1.3505688.

[8] V.R. Buch, A. Kumar, S.K. Rawal, ScienceDirect Review on electrochromic property for WO_3 thin films usingdifferent deposition techniques, Mater. Today Proc. 3 (2016) 1429–1437, https://doi.org/10.1016/j.matpr.2016.04.025.

[9] E. Cazzanelli, G. Mariotto, C. Vinegoni, A. Kuzmin, J. Purans, D. Fisica, U. Calabria, R. Cosenza, Pure Color Centres and Polymorphism in and Mixed (1-x) WO_3.y.xReO_2Powders vol. 5, (1999).

[10] S. Cong, F. Geng, Z. Zhao, Tungsten oxide materials for optoelectronic applications, Adv. Mater. 28 (2016) 10518–10528, https://doi.org/10.1002/adma.201601109.

[11] H. Zheng, J.Z. Ou, M.S. Strano, R.B. Kaner, A. Mitchell, Nanostructured Tungsten Oxide – Properties , Synthesis , and Applications, (2011), pp. 2175–2196, https://doi.org/10.1002/adfm.201002477.

[12] V.A. Online, X. Chang, S. Sun, L. Dong, Y. Dong, Y. Yin, RSC Advances Large-scale production of tungsten trioxide nanoparticles for electrochromic application †, RSC Adv. 4 (2014) 8994–9002, https://doi.org/10.1039/c3ra47733a.

[13] S.K.D. Ã, Opportunities and Challenges in Science and Technology of WO_3 for Electrochromic and Related Applications vol. 92, (2008), pp. 245–258, https://doi.org/10.1016/j.solmat.2007.01.026.

[14] C.K. Wang, C.K. Lin, C.L. Wu, S. Brahma, S.C. Wang, J.L. Huang, Characterization of electrochromic tungsten oxide film from electrochemical anodized RF-sputtered tungsten films, Ceram. Int. 39 (2013) 4293–4298, https://doi.org/10.1016/j.ceramint.2012.11.010.

[15] C.G. Granqvist, M.A. Arvizu, I. Bayrak Pehlivan, H.Y. Qu, R.T. Wen, G.A. Niklasson, Electrochromic materials and devices for energy efficiency and human comfort in buildings: a critical review, Electrochim. Acta 259 (2017) 1170–1182, https://doi.org/10.1016/j.electacta.2017.11.169.

[16] D.S. Martínez, A.M. Cruz, E.L. Cuéllar, Controlled growth of WO_3 nanostructures with three different morphologies and their structural, Optical , and Photodecomposition Studies 398 (2011) 179–186, https://doi.org/10.1016/j.apcata.2011.03.034.

[17] L. Zhang, X. Tang, Z. Lu, Z. Wang, L. Li, Y. Xiao, Applied Surface Science Facile synthesis and photocatalytic activity of hierarchical WO_3 core – shell microspheres, Appl. Surf. Sci. 258 (2011) 1719–1724, https://doi.org/10.1016/j.apsusc.2011.10.022.

[18] L. Jiayin, H. Jianfeng, W. Jianpeng, C. Liyun, K. Yanagisawa, Morphology-controlled synthesis of tungsten oxide hydrates crystallites via a facile , additive-free hydrothermal process, Ceram. Int. 38 (2012) 4495–4500, https://doi.org/10.1016/j.ceramint.2012.02.025.

[19] S. Supothina, P. Seeharaj, S. Yoriya, M. Sriyudthsak, Synthesis of Tungsten Oxide Nanoparticles by Acid Precipitation Method vol. 33, (2007), pp. 931–936, https://doi.org/10.1016/j.ceramint.2006.02.007.

[20] W. Morales, M. Cason, O. Aina, N.R. De Tacconi, K. Rajeshwar, Combustion Synthesis and Characterization of Nanocrystalline WO_3, (2008), pp. 6318–6319.

[21] H. Ahmadian, F. Al Hessari, A.M. Arabi, Preparation and characterization of Luminescent nanostructured Gd_2O_3-Y_2O_3:Eu synthesized by the solution combustion process, Ceram. Int. (2019), https://doi.org/10.1016/j.ceramint.2019.06.106.

[22] K.C. Patil, Advanced ceramics: combustion synthesis and properties, Bull. Mater. Sci. 16 (1993) 533–541, https://doi.org/10.1007/BF02757654.

[23] P. Sharma, G. Singh, Solution-combustion : the versatile route to synthesize silver nanoparticles, J. Nano Res. 13 (2011) 2553–2561, https://doi.org/10.1007/s11051-010-0148-3.

[24] K.V. Manukyan, A. Cross, S. Roslyakov, S. Rouvimov, A.S. Rogachev, E.E. Wolf, A.S. Mukasyan, Solution Combustion Synthesis of Nano-Crystalline Metallic Materials : Mechanistic Studies, (2013).

[25] K. Rajeshwar, N.R. De Tacconi, Solution combustion synthesis of oxide semiconductors for solar energy conversion and environmental remediation, Chem. Soc. Rev. 38 (2009) 1984–1998, https://doi.org/10.1039/b811238j.

[26] S.T. Aruna, A.S. Mukasyan, Combustion synthesis and nanomaterials, Curr. Opin. Solid State Mater. Sci. 12 (2008) 44–50, https://doi.org/10.1016/j.cossms.2008.12.002.

[27] M. Sharbatdaran, A. Novinrooz, H. Noorkojouri, Preparation and characterization of WO_3 electrochromic films obtained by the sol-gel process, Iran, J. Chem. Chem. Eng. 25 (2006) 25–29.

[28] A.K. Nayak, S. Lee, Y.I. Choi, H.J. Yoon, Y. Sohn, D. Pradhan, Crystal phase and size-controlled synthesis of tungsten trioxide hydrate nanoplates at room temperature: enhanced Cr(VI) photoreduction and methylene blue adsorption properties, ACS Sustain. Chem. Eng. 5 (2017) 2741–2750, https://doi.org/10.1021/acssuschemeng.6b03084.

[29] A.K. Nayak, Y. Sohn, D. Pradhan, Facile green synthesis of WO_3·H_2O nanoplates and WO_3 nanowires with enhanced photoelectrochemical performance, Cryst. Growth Des. 17 (2017) 4949–4957, https://doi.org/10.1021/acs.cgd.7b00886.

[30] M. Breedon, P. Spizzirri, M. Taylor, J. Plessis, Synthesis of nanostructured tungsten oxide thin Films : a simple , controllable , inexpensive, Aqueous Sol-Gel Method 4

(2010) 1–10, https://doi.org/10.1021/cg9010295.
[31] M.R. Khodadadi, M.E. Olya, A. Naeimi, AUTHOR ' S PROOF Highly Efficient Al-Doped ZnO : Ag Catalyst for RB19 Photocatalytic Degradation : Microwave-Assisted Synthesis and Characterization vol. 32, (2016), pp. 1–9, https://doi.org/10.1007/s11814-016-0001-1.
[32] K.C. Patil, Chemistry of Nanocrystalline Oxide Materials, Combustion Synthesis, Properties and Applications, (2008).
[33] S. Rasouli, A. Masoud, A. Alireza, N. Seyed, M. Hashemi, Microwave-Assisted combustion synthesis of ZnO : Eu Nanoparticles : effect of fuel types, J. Fluoresc. 0 (2017) 0, https://doi.org/10.1007/s10895-017-2179-y.
[34] T. Vogt, P.M. Woodward, B.A. Hunter, The High-Temperature Phases of WO_3 vol. 215, (1999), pp. 209–215.
[35] M. Ahmadi, R. Younesi, M.J.-F. Guinel, Synthesis of tungsten oxide nanoparticles using a hydrothermal method at ambient pressure, J. Mater. Res. 29 (2014) 1424–1430, https://doi.org/10.1557/jmr.2014.155.
[36] S. Cong, F. Geng, Z. Zhao, Tungsten Oxide Materials for Optoelectronic Applications, (2016), https://doi.org/10.1002/adma.201601109.
[37] D.B. Hernandez-uresti, D. Sánchez-martínez, A.M. Cruz, Characterization and photocatalytic properties of hexagonal and monoclinic WO_3 prepared via microwave-assisted hydrothermal synthesis, Ceram. Int. 40 (2014) 4767–4775, https://doi.org/10.1016/j.ceramint.2013.09.022.
[38] N. Sharma, M. Deepa, P. Varshney, S.A. Agnihotry, FTIR investigations of tungsten oxide electrochromic films derived from organically modified peroxotungstic acid precursors, Thin Solid Films 401 (2001) 45–51.
[39] C. El, Synthesis and characterization of macroporous tungsten oxide films for electrochromic application, J. Sol. Gel Sci. Technol. 28 (2003) 235–244.
[40] J.L. Solis, A. Hoel, V. Lantto, C.G. Granqvist, Infrared spectroscopy study of electrochromic nanocrystalline tungsten oxide films made by reactive advanced gas deposition Infrared spectroscopy study of electrochromic nanocrystalline tungsten oxide films made by reactive advanced gas deposition, J. Appl. Phys. 89 (2001) 2727, https://doi.org/10.1063/1.1343520.
[41] J.C. Toniolo, M.D. Lima, A.S. Takimi, C.P. Bergmann, Synthesis of alumina powders by the glycine-nitrate combustion process, Mater. Res. Bull. 40 (2005) 561–571, https://doi.org/10.1016/j.materresbull.2004.07.019.
[42] H.C. Warad, S.C. Ghosh, B. Hemtanon, C. Thanachayanont, J. Dutta, Luminescent nanoparticles of Mn doped ZnS passivated with sodium hexametaphosphate, Sci. Technol. Adv. Mater. 6 (2005) 296–301, https://doi.org/10.1016/j.stam.2005.03.006.
[43] V. Soleimanian, S.R. Aghdaee, Applied Surface Science the influence of annealing temperature on the slip plane activity and optical properties of nanostructured ZnO films, Appl. Surf. Sci. 258 (2011) 1495–1504, https://doi.org/10.1016/j.apsusc.2011.09.115.
[44] R.M.P.P. Sahay, Effect of precursors on the microstructural , optical , electrical and electrochromic properties of WO_3 nanocrystalline thin films, J. Mater. Sci. Mater. Electron. 26 (2015) 6293–6305, https://doi.org/10.1007/s10854-015-3216-8.
[45] M. Feng, A.L. Pan, H.R. Zhang, Z.A. Li, F. Liu, H.W. Liu, D.X. Shi, Strong Photoluminescence of Nanostructured Crystalline Tungsten Oxide Thin Films, (2005), pp. 14–16, https://doi.org/10.1063/1.1898434.
[46] V. Madhavi, P. Kondaiah, O.M. Hussain, S. Uthanna, Structural , optical and electrochromic properties of RF magnetron sputtered WO_3 thin fi lms, Phys. B Phys. Condens. Matter. 454 (2014) 141–147, https://doi.org/10.1016/j.physb.2014.07.029.
[47] S.K. Deb, Optical and photoelectric properties and colour centres in thin films of tungsten oxide, Philos. Mag. 27 (1973) 801–822, https://doi.org/10.1080/14786437308227562.
[48] F. Wang, C. Di Valentin, G. Pacchioni, Electronic and structural properties of WO_3: a systematic hybrid DFT study, J. Phys. Chem. C 115 (2011) 8345–8353, https://doi.org/10.1021/jp201057m.
[49] J. Zhu, M. Vasilopoulou, D. Davazoglou, S. Kennou, A. Chroneos, U. Schwingenschlögl, Intrinsic defects and H doping in WO_3, Sci. Rep. 7 (2017) 1–9, https://doi.org/10.1038/srep40882.
[50] H. Search, C. Journals, A. Contact, M. Iopscience, I.O.P. Conf, I.P. Address, Studies on the Uv- Visible and Photoluminescent Emission in Nanocrystalline Tungsten Oxide, 012119 (n.d.) 2–6. doi:10.1088/1757-899X/73/1/012119.
[51] M.B. Johansson, G. Baldissera, I. Valyukh, C. Persson, H. Arwin, G.A. Niklasson, L. Österlund, Electronic and optical properties of nanocrystalline WO_3 thin films studied by optical spectroscopy and density functional calculations, J. Phys. Condens. Matter 25 (2013), https://doi.org/10.1088/0953-8984/25/20/205502.
[52] M.B. Johansson, B. Zietz, G.A. Niklasson, L. Österlund, Optical Properties of Nanocrystalline WO_3 and WO_{3-X} Thin Films Prepared by DC Magnetron Sputtering 213510, (2014), https://doi.org/10.1063/1.4880162.
[53] S.K. Kansal, N. Kaur, S. Singh, Photocatalytic degradation of two commercial reactive dyes in aqueous phase using nanophotocatalysts, Nanoscale Res. Lett. 4 (2009) 709–716, https://doi.org/10.1007/s11671-009-9300-3.
[54] R. Kumar, J. Rashid, M.A. Barakat, Zero valent Ag deposited TiO_2 for the efficient photocatalysis of methylene blue under UV-C light irradiation, Colloids Interface Sci. Commun. 5 (2015) 1–4, https://doi.org/10.1016/j.colcom.2015.05.001.
[55] H. Huang, D.Y.C. Leung, P.C.W. Kwong, J. Xiong, L. Zhang, Enhanced photocatalytic degradation of methylene blue under vacuum ultraviolet irradiation, Catal. Today 201 (2013) 189–194, https://doi.org/10.1016/j.cattod.2012.06.022.
[56] E.M. Saggioro, A.S. Oliveira, T. Pavesi, C.G. Maia, L.F.V. Ferreira, J.C. Moreira, Use of titanium dioxide photocatalysis on the remediation of model textile wastewaters containing azo dyes, Molecules 16 (2011) 10370–10386, https://doi.org/10.3390/molecules161210370.
[57] M.E. Olya, A. Pirkarami, Cost-effective photoelectrocatalytic treatment of dyes in a batch reactor equipped with solar cells, Separ. Purif. Technol. 118 (2013) 557–566, https://doi.org/10.1016/j.seppur.2013.07.038.
[58] J. Tarver, J.E. Yoo, Y.-L. Loo, Organic electronic devices with water-dispersible conducting polymers, Compr. Nanosci. Technol. (2011) 413–446, https://doi.org/10.1016/B978-0-12-374396-1.00136-7.
[59] J. Yin, H. Cao, J. Zhang, M. Qu, Z. Zhou, Synthesis and applications of γ - tungsten oxide hierarchical nanostructures, Cryst. Growth Des. 13 (2013) 3–13.
[60] H. Pang, X. Xiang, Z. Li, Y. Fu, X. Zu, I. Recently, Hydrothermal synthesis and optical applications and materials science properties of hexagonal tungsten oxide nanocrystals assisted by ammonium tartrate, Phys. Status Solidi A 209 (2012) 537–544, https://doi.org/10.1002/pssa.201127456.